ACS NANO

www.acsnano.org

ARTICLE

Ultrathin 2D As_2Se_3 Nanosheets for Photothermal-Triggered Cancer Immunotherapy

Jingyi Zhang, Yue Qin, Yiming Chen, Xinyang Zhao, Jing Wang, Zhenzhen Wang, Jiayi Li, Jing Zhao, Shengjin Liu, Zijian Guo, Wei Wei,* Jing Zhao,* and Xiuxiu Wang*

Cite This: *ACS Nano* 2024, 18, 4398−4413

Read Online

ACCESS | Metrics & More | Article Recommendations | Supporting Information

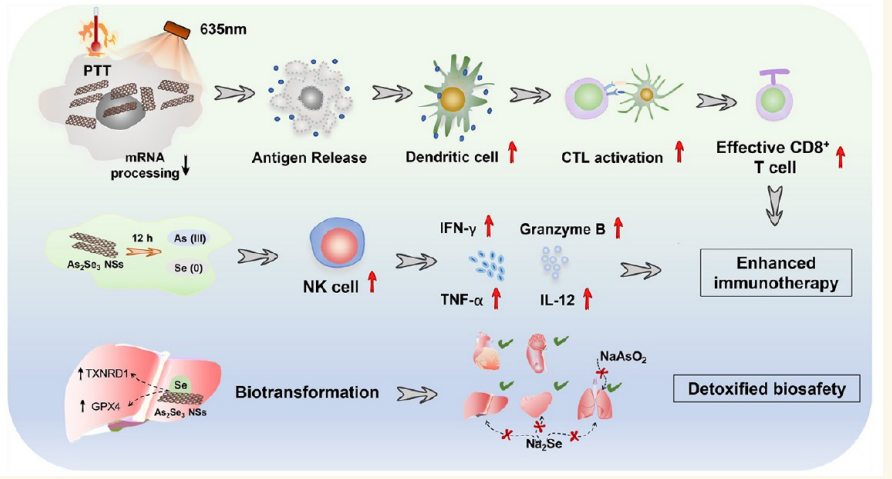

ABSTRACT: Arsenic trioxide (As_2O_3) has achieved groundbreaking success in the treatment of acute promyelocytic leukemia (APL). However, its toxic side effects seriously limit its therapeutic application in the treatment of solid tumors. To detoxify the severe side effects of arsenic, herein we synthesized innovative 2D ultrathin As_2Se_3 nanosheets (As_2Se_3 NSs) with synergistic photothermal-triggered immunotherapy effects. As_2Se_3 NSs are biocompatible and biodegradable under physiological conditions and can release As(III) and Se(0). Furthermore, selenium increases the immunomodulatory efficacy of arsenic treatments, facilitating reprogramming of the tumor microenvironment by As_2Se_3 NSs by enhancing the infiltration of natural killer cells and effector tumor-specific $CD8^+$ T cells. The synergistic combination of photothermal therapy and immunotherapy driven by As_2Se_3 NSs via a simple but effective all-in-one strategy achieved efficient anticancer effects, addressing the key limitations of As_2O_3 for solid tumor treatment. This work demonstrates not only the great potential of selenium for detoxifying arsenic but also the application of 2D As_2Se_3 nanosheets for cancer therapy.

KEYWORDS: *2D arsenic selenide, detoxification, biotransformation, immunotherapy, photothermal therapy*

INTRODUCTION

Arsenic drugs have become the first-line therapy in the clinic owing to their outstanding efficacy in treating acute promyelocytic leukemia (APL).[1,2] The complete remission rate of APL patients following arsenic trioxide (As_2O_3) treatment is approximately 83−95%, and this treatment has attracted widespread attention from the scientific community for arsenic-based antitumor drugs.[3] However, the contradiction between the high efficacy and high systemic toxicity of arsenic drugs seriously limits its clinical therapeutic efficacy in solid tumor treatment.[2,4]

Received: October 24, 2023
Revised: January 20, 2024
Accepted: January 22, 2024
Published: January 26, 2024

https://doi.org/10.1021/acsnano.3c10432
ACS Nano 2024, 18, 4398−4413

Scheme 1. Schematic Illustration of the As_2Se_3 Nanosheets with Excellent Biosafety, Bioavailability, Photothermal Conversion Efficiency, and Immune Microenvironment Remodeling Capabilities Enhanced the Synergistic Photothermal Therapy and Immunotherapy for Solid Tumor Therapy *Via* an All-in-One Strategy[a]

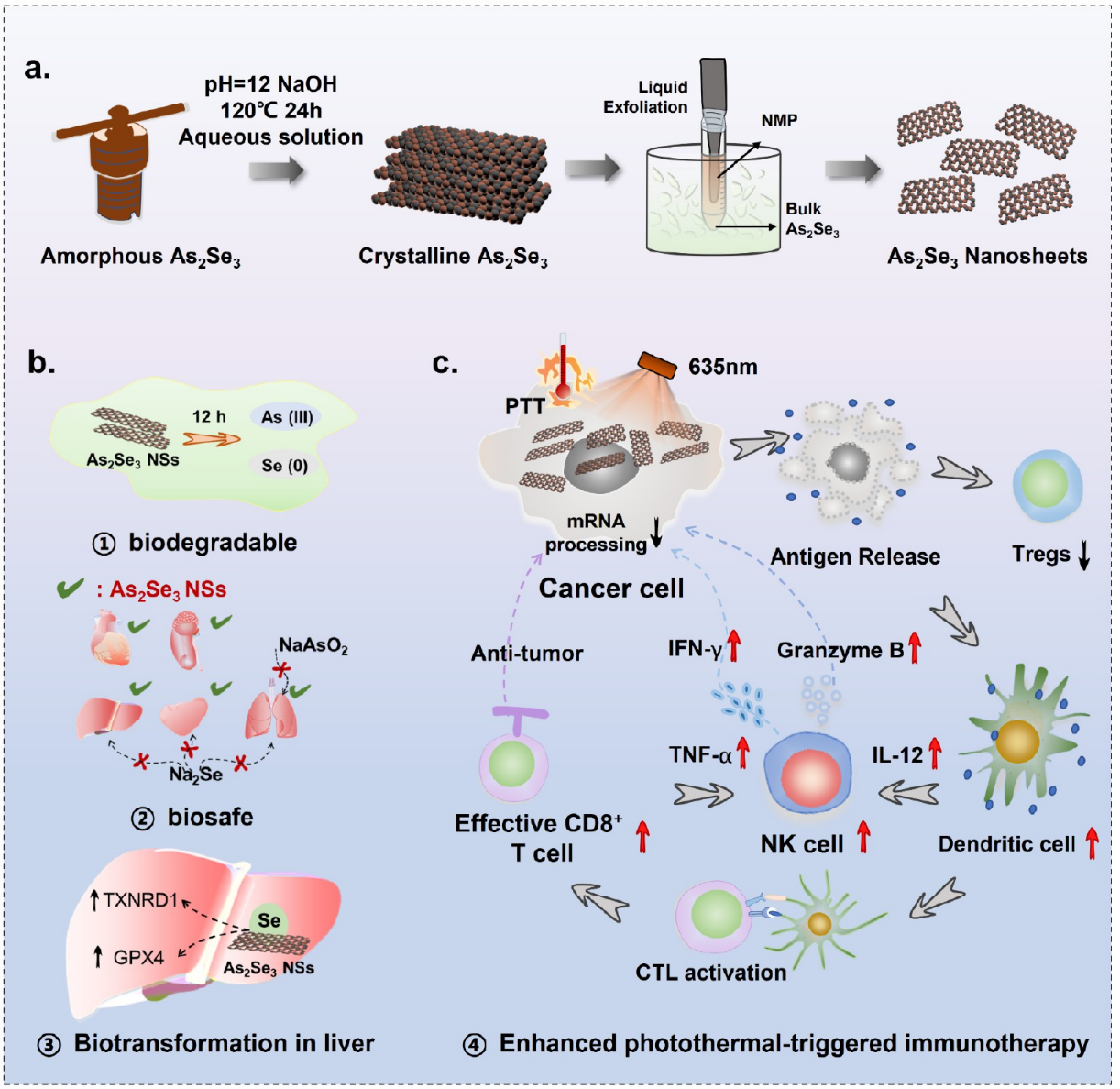

[a](a) Synthesis process of As_2Se_3 NSs *via* high-pressure crystallization and a liquid-phase exfoliation strategy. (b) Detoxified biosafety of As_2Se_3 NSs *in vivo*. (c) Enhanced photothermal-triggered immunotherapy of As_2Se_3 NSs *in vivo*.

The chemical form of arsenic determines the mode of toxicity.[5] Trivalent arsenic is generally considered to be more toxic than pentavalent arsenic. Among inorganic arsenic agents, arsenic trioxide (As_2O_3) is one of the most toxic forms of natural arsenic.[6] However, As_2O_3 also produces strong side effects, such as liver damage and prolongation of the QTc interval on electrocardiography (ECG).[7,8] Many excellent efforts have been made by Gao et al. and Ma et al. to overcome these limitations, including the development of multifunctional drug delivery systems, such as hollow silica-, low-attachment peptide-, or poly(lactic-*co*-glycolic acid) (PLGA)-modified As_2O_3-based multifunctional drug delivery systems,[9−11] especially ferritin-delivery arsenic nanomedicines with very high cancer cell-binding affinity and high arsenic delivery efficiency.[12] However, the additional drug delivery platforms have raised continual concerns about the inevitable cumulative burden on the liver and the corresponding lack of overdose detoxification mechanisms.[13−16] These dilemmas emphasize the desperate need to develop some strategies to efficiently detoxify arsenic and enhance its therapeutic effect.

Fortunately, selenium (Se), an essential trace element involved in maintaining human health, was shown to have a mutual detoxification relationship with arsenic.[17−19] A reliable detoxification mechanism in the body involves the reaction of arsenic and selenium in the liver, which accelerates their excretion in bile.[20] Moreover, the intake of selenium at the nutritional level reduces cancer incidence by regulating immune functions through the diverse redox-regulating activities of selenoproteins, reversing the immunosuppression of the tumor microenvironment to promote an antitumor immune-activating

https://doi.org/10.1021/acsnano.3c10432
ACS Nano 2024, 18, 4398−4413

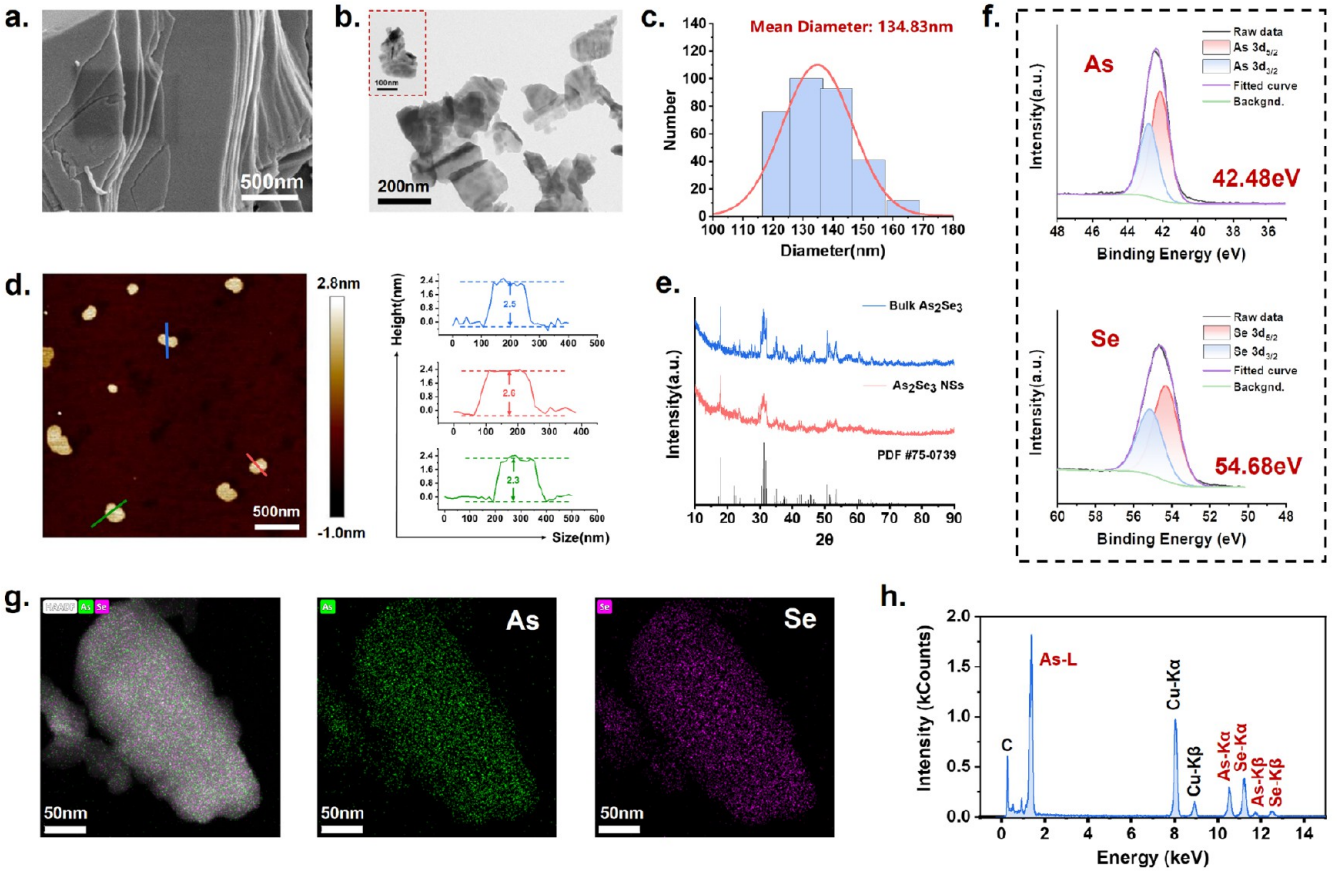

Figure 1. Characterization of As_2Se_3 NSs. (a) SEM image of bulk As_2Se_3 after high-pressure crystallization. (b) TEM image, (c) particle diameter distribution, (d) AFM image, (e) XRD pattern, (f) XPS spectrum, and (g, h) EDS spectrum of the As_2Se_3 NSs.

status.[21−23] Pioneering work by Chen et al. on the development of Se-based therapy revealed the tremendous potential of Se in reprogramming the immune microenvironment of lung adenocarcinoma, generating vaccine nanoadjuvants, attenuating allergic dermatitis, recognizing metallodrugs, and reinvigorating cancer radioimmunotherapy.[24−29] A promising combination of selenium and arsenic to form As_2Se_3 could be an excellent strategy for lowering the toxic effects and increasing the therapeutic and immunomodulatory efficacy of arsenic treatments.

As a type of arsenide chalcogenide, As_2X_3 (X = S, Se, and Te) is predicted to be a semiconductor with anisotropic carrier mobilities, optical properties, intrinsic ferroelectricity, and equivalent stripping energy to graphene.[30−32] As_2Se_3 is a bulk-layered crystal with monoclinic structures similar to those of As_2S_3 and is widely used as an electrophotographic photoconductor.[33,34] Layered two-dimensional (2D) materials have achieved excellent therapeutic effects in antitumor therapy due to their outstanding optical properties.[35−37] Importantly, layered two-dimensional (2D) arsenic nanomaterials have shown large success in the application of electronic devices, energy systems, and cancer therapy.[15,38−42] In addition, the typical ultrathin layered structure of two-dimensional nanomaterials provides outstanding in-plane electron mobilities and adjustable bandgaps to achieve high photothermal conversion efficiencies.[43,44] This hyperthermic mode converts light energy into thermal energy to engender noninvasive photothermal therapy (PTT).[44] Notably, the calculated indirect bandgap of bilayer As_2Se_3 was 2.202 eV, which is similar to that of single-layered black phosphorus (2.0 eV).[30,45] To endow As_2Se_3 with a controlled material topography and multifunctional properties, layered 2D As_2Se_3 nanosheets are extremely promising. However, little effort has been devoted to the synthesis of 2D As_2Se_3 nanosheets.

In light of these considerations, in this work, we successfully synthesized arsenic selenide nanosheets (As_2Se_3 NSs) by liquid exfoliation after high-temperature crystallization, and the resulting material exhibited excellent photothermal conversion efficiency. This hyperthermia improved the immunogenicity of the tumor and created a favorable niche for tumor-infiltrating lymphocyte (TIL) recruitment, thereby facilitating Se-mediated immunotherapy. Importantly, compared with $NaAsO_2$ and Na_2Se, As_2Se_3 NSs are biocompatible and biosafe when degraded under physiological conditions to release As(III) and Se(0), and the coexistence of Se and As reduces the systemic toxicity of As_2Se_3 NSs. The selenium derived from these biodegradable As_2Se_3 NSs promotes the conversion of Se to selenoenzymes in the liver, further preventing the oxidative damage induced by As. Furthermore, the addition of Se enhances the therapeutic effect of As_2Se_3 NSs by reprogramming the tumor microenvironment (TME) through the infiltration of natural killer (NK) cells and effector tumor-specific $CD8^+$ T cells. The resulting As_2Se_3 NSs, which have high biocompatibility, detoxifying capability, biosafety and bioavailability, photothermal conversion efficiency, and immune microenvironment reshaping ability, led to great enhancement of synergistic photothermal therapy and immunotherapy via an all-in-one strategy.

https://doi.org/10.1021/acsnano.3c10432
ACS Nano 2024, 18, 4398−4413

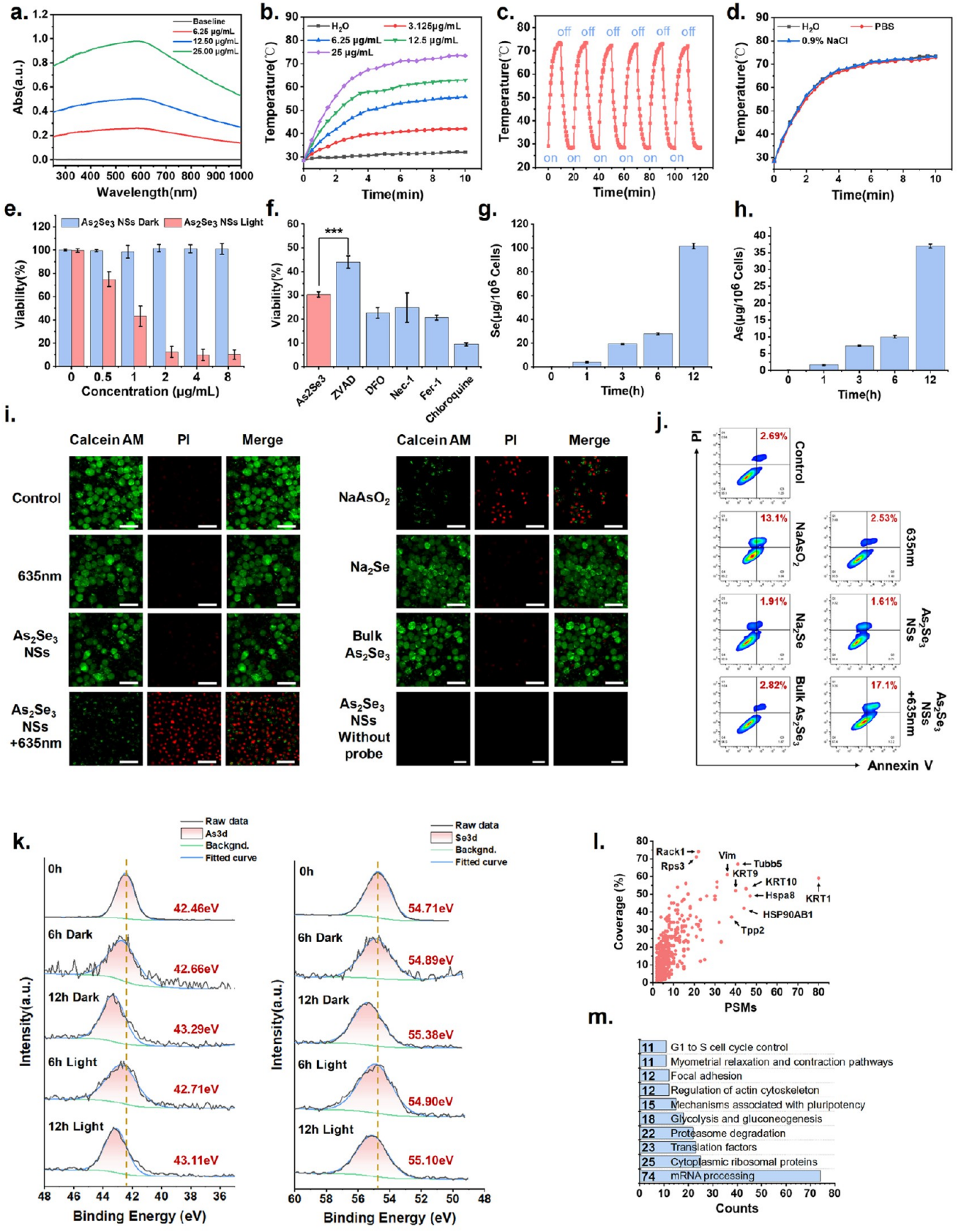

Figure 2. PTT effect and antitumor mechanism analysis of As_2Se_3 NSs. (a) UV spectrum of As_2Se_3 NSs. (b) Temperature changes in As_2Se_3 NSs at different concentrations with a 635 nm NIR laser at 2.0 W/cm^2 for 10 min. (c) Photothermal stability of As_2Se_3 NSs for six on/off irradiation cycles. (d) Changes in the temperature of As_2Se_3 NSs in different physiological buffers. (e) Viability of 4T1 cells cultured with As_2Se_3 NSs with or without 635 nm NIR laser (2.0 W/cm^2) irradiation for 10 min. (f) Viability of 4T1 cells cultured with As_2Se_3 NSs and different cell death inhibitors. (g, h) The uptake of As_2Se_3 NSs was detected by ICP−MS *in vitro*. (i) Calcein AM (green) and PI (red) staining of 4T1 cells after

https://doi.org/10.1021/acsnano.3c10432
ACS Nano 2024, 18, 4398−4413

Figure 2. continued

thermal therapy *in vitro* was captured by fluorescence microscopy. (j) Apoptosis analysis of 4T1 cells by flow cytometry after different treatments. (k) XPS detection of the change in valence of As and Se. (l) The binding partners of As_2Se_3 NSs and (m) the enrichment pathways affected by As_2Se_3 NSs in cancer cells.

RESULTS AND DISCUSSION

Synthesis and Characterization of As_2Se_3 NSs. The therapeutic effect of 2D materials is highly anticipated, demonstrating excellent potential as a pharmaceutical platform.[46] The liquid exfoliation method is the preferred strategy for the preparation of high-quality 2D materials because of its mild operation conditions.[47,48] In this work, arsenic selenide was first crystallized under high pressure in an alkaline solution and subsequently exfoliated in *N*-methylpyrrolidone (NMP) to synthesize As_2Se_3 nanosheets (As_2Se_3 NSs) (Scheme 1a and Figure S1). Scanning electron microscopy (SEM) results indicated that after high-pressure crystallization in alkaline solution, amorphous arsenic selenide powder can be transformed into layered stacked crystals (Figure 1a). Based on the relationship between the stripping energy and solvent polarity, As_2Se_3 NSs were successfully synthesized by exfoliation in NMP, as indicated by the transmission electron microscopy (TEM) images (Figure 1b). The effective particle size of the As_2Se_3 NSs was approximately 134.83 nm, as determined via dynamic light scattering (DLS) detection, which was consistent with the TEM image (Figure 1c).

The thickness of 2D materials significantly affects the photoelectric properties of nanoparticles by modulating the bandgap width, and the thickness of As_2Se_3 NSs, as detected by atomic force microscopy (AFM), was approximately 2.5 nm, which was twice the theoretical value of 12.096 Å for the single-layer arsenic selenide *a*-axis (Figure 1d). Based on these findings, we determined that the synthesized As_2Se_3 nanosheets were composed of bilayers. Furthermore, the indirect bandgap of As_2Se_3 NSs detected by UV−visible diffuse reflectance spectroscopy (UV−Vis-DRS) was 1.65 eV (Figure S 1d), indicating good optical properties.[49]

The compositions of As_2Se_3 NSs and the As_2Se_3 precursor were detected via X-ray diffraction (XRD). Both the As_2Se_3 NSs and the As_2Se_3 precursor were determined to be As_2Se_3, consistent with Joint Committee on Powder Diffraction Standards (JCPDS) 75-0739 (Figure 1e). Next, by X-ray photoelectron spectroscopy (XPS), the binding energy of the As 3d orbital was 42.48 eV, whereas that of the Se 3d orbital was 54.68 eV, indicating the charges of As(III) and Se(II) (Figure 1f). In addition, energy-dispersive spectroscopy (EDS) confirmed the colocalization of As and Se (Figure 1g). The spectrum showed clear peaks corresponding to As and Se, and the semiquantitative results indicated that the ratio of As/Se was ≈2:3 (Figure 1h and Table S1), which was further confirmed by inductively coupled plasma mass spectrometry (ICP−MS) (Table S2).

In Vitro Studies of Photothermal As_2Se_3 NSs. The indirect bandgap of bilayer As_2Se_3 was 1.65 eV, which endowed As_2Se_3 NSs with potential photothermal conversion efficiency. This photothermal conversion was then investigated. First, the UV spectrum showed that As_2Se_3 NSs exhibited broad peak absorption near 600 nm (Figure 2a). Considering the spectral and laser tissue penetrability, a 635 nm laser was chosen for photothermal conversion of As_2Se_3 NSs. Within 10 min, the temperature of the As_2Se_3 NSs (25 μg/mL) reached 73.4 °C at 2.0 W cm^{-2} while maintaining stability for 6 cycles (Figure 2b,c and Figure S2). Afterward, in physiological buffer, the photothermal conversion of As_2Se_3 NSs was maintained at the same efficiency as that in water (Figure 2d). Moreover, the photothermal conversion efficiency of As_2Se_3 NSs was determined via a common method, and the η value of As_2Se_3 NSs was 39.85%, which was higher than that of most reported PTT agents (Figure S2c).[50−52]

Considering the high photothermal conversion capability of As_2Se_3 NSs *in vitro*, we then tested the photothermal therapeutic effect of As_2Se_3 NSs on cells. Breast cancer is the most common cancer and has the highest mortality rate; thus, effective treatment is urgently needed.[53] Thus, in this work, the mouse breast cancer cell line 4T1 was selected, and the cytotoxicity of As_2Se_3 NSs was evaluated in 4T1 cells. As the crucial constituent elements in As_2Se_3 NSs, the corresponding single-element salts $NaAsO_2$ and Na_2Se were selected for comparison of two reactive valence ions, while bulk As_2Se_3 was selected as a control to offset the advantages of the 2D As_2Se_3 structure (Figure S3a). As shown, the IC_{50} value of the As_2Se_3 NSs was 0.79 ± 0.27 μg/mL with 635 nm laser irradiation and 17.51 ± 1.09 μg/mL without irradiation. The phototoxic index (PI) of As_2Se_3 NSs was 22.16, indicating a significant difference in phototoxicity and emphasizing the PTT effect of As_2Se_3 NSs in killing cancer cells (Figure 2e and Figure S3b). In comparison, the IC_{50} value of $NaAsO_2$ was 1.47 ± 0.08 μg/mL (Figure S3a). Moreover, this cytotoxicity was verified through calcein AM and propidium iodine staining (Figure 2i). Next, the mode of cell death induced by As_2Se_3 NSs after irradiation was elucidated through the addition of cell death inhibitors, and this cell death was rescued by the apoptosis inhibitor Z-VAD-FMK, indicating that As_2Se_3 NSs induced apoptosis (Figure 2f). Apoptosis was further confirmed through Annexin V and propidium iodide staining. As shown, both As_2Se_3 NSs+635 nm and $NaAsO_2$ induced 4T1 cell apoptosis (Figure 2j).

Stability and Mechanism of As_2Se_3 NSs In Vitro. To thoroughly elucidate the action of As_2Se_3 NSs under physiological conditions, we first examined the oxidative degradation of As_2Se_3 NSs at 37 °C. As a result, more than 50% of the As(III) was released and became soluble within 72 h, while less than 0.5% of the Se could be detected in aqueous solution; this percentage was speculated to be Se(0) (Figure S3c,d). The degradable release of soluble As(III) from As_2Se_3 NSs ultimately contributes to the cytotoxicity of the As_2Se_3 NSs. The TEM and EDS results indicated that the As_2Se_3 NSs gradually disintegrated and aggregated in water, and the Se/As ratio gradually increased (Figure S3e−g). These results emphasized the biodegradability of As_2Se_3 NSs under physiological conditions after 12 h. As the uptake of As_2Se_3 NSs significantly increased (as indicated by the As and Se contents) after 12 h (Figure 2g,h), we then evaluated the valence states of As and Se by XPS at different reaction times and found that both valence states of As and Se increased after 12 h, indicating the oxidation of As and Se in As_2Se_3 NSs under physiological conditions (Figure 2k).

This oxidation of As_2Se_3 NSs was found to affect biological pathways in cancer cells after As_2Se_3 NSs treatment, and the

https://doi.org/10.1021/acsnano.3c10432
ACS Nano 2024, 18, 4398−4413

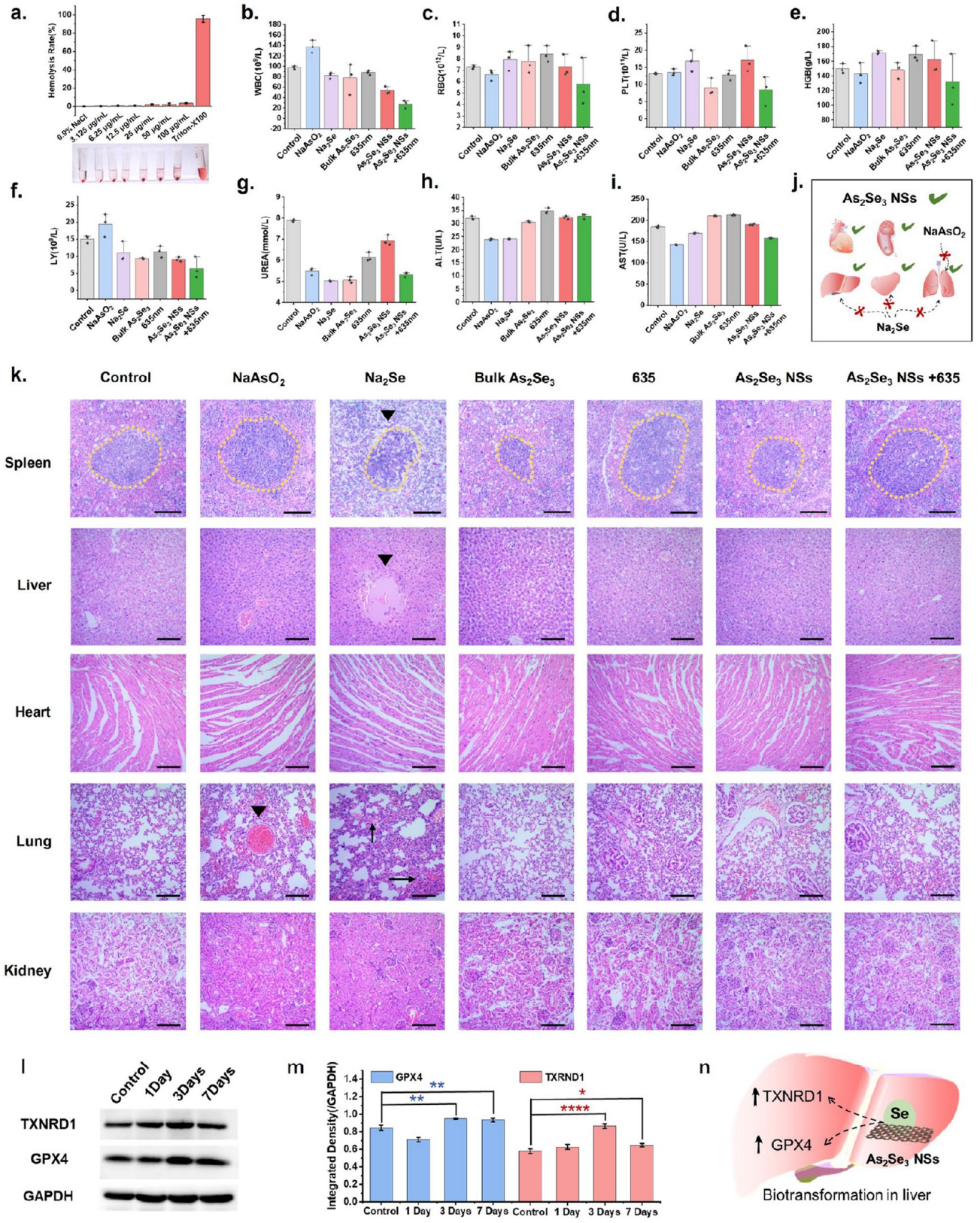

Figure 3. Biosafety of As_2Se_3 NSs combined with PTT *in vivo*. (a) Hemolysis analysis of As_2Se_3 NSs. (b–f) Blood hematological and (g–i) biochemical analyses of mice that received repetitive treatments at different dosages. (j) Schematic of organ toxicity induced by As_2Se_3 NSs compared with that induced by $NaAsO_2$ and Na_2Se. (k) Pathological analysis of the spleen, liver, heart, lung, and kidney by H&E staining; scale bar: 100 μm. (l) Western blot analysis of the expression of TXNR1 and GPX4 in liver tissues from mice injected with As_2Se_3 NSs for 1, 3, and 7 days. (m) Integrated density of the bands determined via Western blot analysis. (n) Schematic of the biotransformation of As_2Se_3 NSs. All the

https://doi.org/10.1021/acsnano.3c10432
ACS Nano 2024, 18, 4398–4413

Figure 3. continued

values are expressed as the means ± SDs of triplicate samples. Statistical significance was assessed by one-way ANOVA. $P < 0.05$ (*), $P < 0.01$ (**), $P < 0.001$ (***), or $P < 0.0001$ (****).

interaction between As_2Se_3 NSs and intracellular proteins was also an important factor affecting the mechanism of cell death. Therefore, the cellular binding proteins of As_2Se_3 NSs were subsequently identified. After extraction of the protein coronas adsorbed on As_2Se_3 NSs, the binding proteins were then analyzed via protein mass spectrometry profiling (Figures S4−S6). As a result, the protein with the most reliable peptide was the cytoskeleton protein KRT1, followed by the Hspa8 protein, which participates in a variety of cell processes and the correct folding of the proteome (Figure 2l and Table S3).[54] Then, according to the bioinformatic enrichment analysis by wikipathways, the pathways enriched in the most abundant binding proteins were mRNA processing, followed by cytoplasmic ribosomal proteins and translation factors, all pointing to the translation process of proteins (Figure 2m). These results indicated that after irradiation, As_2Se_3 NSs bind to proteins involved in glycolysis, cytoskeleton regulation, and the cell cycle, affecting the protein translation process in cells.

Excellent Biosafety, Detoxifying Capability, and Bioavailability of As_2Se_3 NSs under Therapeutic Conditions. Biosafety and biocompatibility are the primary evaluation criteria for nanomaterials for further therapeutic investigation *in vivo*. In this work, the detoxification effect of the combination of As, which has a high anticancer efficacy, and Se, which has a detoxification function, was also confirmed. First, the hemolysis rate of As_2Se_3 NSs was determined, and the excellent hemolytic properties confirmed the biological safety and bioavailability of As_2Se_3 NSs when they were injected through the tail vein (Figure 3a). Then, a 4T1 tumor-bearing mouse model was constructed, and the model mice were divided into 7 groups. After tail vein injection of saline, $NaAsO_2$, Na_2Se, bulk As_2Se_3, As_2Se_3 NSs, 635 nm irradiation or As_2Se_3 NSs + 635 nm irradiation at an arsenic concentration of 15 mg/kg for 14 days, the results revealed no observable abnormalities in routine blood or biochemical analyses after As_2Se_3 NSs treatment, while a sharp increase in the number of white blood cells and percentage of lymphocytes was observed with $NaAsO_2$ treatment, indicating that the acute inflammatory reaction induced by toxic $NaAsO_2$ can be significantly reduced with the addition of detoxified selenium to As_2Se_3 NSs (Figure 3b−i). This reduction probably originated from the reaction of arsenic and selenium in the liver, accelerating excretion in bile and preventing the excessive accumulation of As. Importantly, evaluations of metabolic excretion via blood, urine, and feces further confirmed the rapid and efficient excretion of As after 24 h (Figure S7). Furthermore, we tested the enrichment of As_2Se_3 NSs by ICP−MS, which demonstrated the degradation of As_2Se_3 over time in various organs (Figure S8). Thus, the coexistence of Se and As in As_2Se_3 NSs reduced the systematic toxicity in this work. In addition, hematoxylin and eosin (H&E) staining of crucial organs further demonstrated the ability of As_2Se_3 NSs to ameliorate the severe damage to the spleen, liver, lungs, and kidney caused by Na_2Se and the severe liver, lung, and kidney damage caused by $NaAsO_2$ (Figure 3j,k and Figure S9). All of these results confirmed the excellent biosafety and detoxifying ability of As_2Se_3 NSs in improving acute and long-term toxicity under therapeutic conditions, overcoming the key challenges of using arsenic drugs for solid tumor treatment.

As an essential trace element that is bioavailable when present as a selenozyme, selenium mediates the regulation of vital redox processes to prevent excessive oxidative damage. Under physiological conditions, the biodegradation of As_2Se_3 NSs to form Se(0) may promote the conversion of Se to selenoenzymes in the liver. Notably, GPX4 and TXNRD1 are two main selenoenzymes that are responsible for the reduction of hydroperoxide and the regulation of cellular redox reactions, growth, and differentiation.[55,56] Thus, to confirm the conversion of selenium in the liver, we evaluated the biotransformation formulations of selenium after intravenous injection of As_2Se_3 NSs for 1, 3, and 7 days. As displayed in Figure 3l,m, compared with those in noninjected mice, the expression of GPX4 and TXNRD1 in treated mice was significantly upregulated after 3 days but slightly increased after 7 days. The elevated expression of GPX4 and TXNRD1 demonstrated that the selenium derived from As_2Se_3 NSs in the liver was readily bioavailable, and this biotransformation decreased with the excretion of As_2Se_3 NSs over time (Figure 3n). Moreover, this biotransformation of selenium to selenoenzymes GPX4 and TXNRD1 further relieves the oxidative damage induced by As in the liver.

The Photothermal and Antitumor Immune Modulating Capabilities of As_2Se_3 NSs. As an excellent photothermal agent, the photothermal effect of As_2Se_3 NSs was investigated *in vivo* (Figure 4a). As displayed in Figure 4b, the temperature of the illuminated tumor site was monitored by photothermal imaging after As_2Se_3 NSs injection, and the temperature of the tumor increased from 37.8 to 51.4 °C in 5 min, indicating that the As_2Se_3 NSs also achieved excellent photothermal effects *in vivo* (Figure 4c).

Encouraged by the immune-regulating functions of Se in reversing immunosuppression to achieve antitumor immune-activating status and reprogramming the immune microenvironment,[21,26−28] hyperthermia improved the immunogenicity of tumors and created a favorable niche for tumor-infiltrating lymphocyte (TIL) recruitment,[57,58] thereby facilitating Se-mediated immunotherapy. The immune-modulating capabilities of Se-based As_2Se_3 NSs in cancer therapy were subsequently explored.

After the administration of saline, $NaAsO_2$, Na_2Se, bulk As_2Se_3, As_2Se_3 NSs, 635 nm irradiation, or As_2Se_3 NSs + 635 nm irradiation to 4T1 tumor-bearing mice for 24 h, the dendritic cells (DCs) in the lymph nodes were first separated. The percentage of $CD80^+$ and $CD86^+$ DCs was significantly elevated to 15% after As_2Se_3 NSs+635 nm treatment, indicating obvious activation of antigen presentation and processing. In this process, DC maturation was also activated in $NaAsO_2$ (Figure 4d and Figure S10a), which is consistent with the reported role of arsenic in inducing acute immune responses.[16] Next, T cells in the lymph nodes were detected by CD69 labeling. As shown, T cells were evaluated after treatment with bulk As_2Se, 635 nm, As_2Se_3 NSs, or As_2Se_3 NSs+635 nm. Although a lower level of $CD4^+$ T cells was produced in the As_2Se_3 NSs group than in the bulk As_2Se_3 group, the 2-fold increase in the number of anticancer $CD8^+$ T cells demonstrated the effective activation of effector anticancer activity by As_2Se_3 NSs (Figure 4e−f and Figure S10b). Most importantly, the activation of DCs and T cells by As_2Se_3 NSs+635 nm was the most significant among the

https://doi.org/10.1021/acsnano.3c10432
ACS Nano 2024, 18, 4398−4413

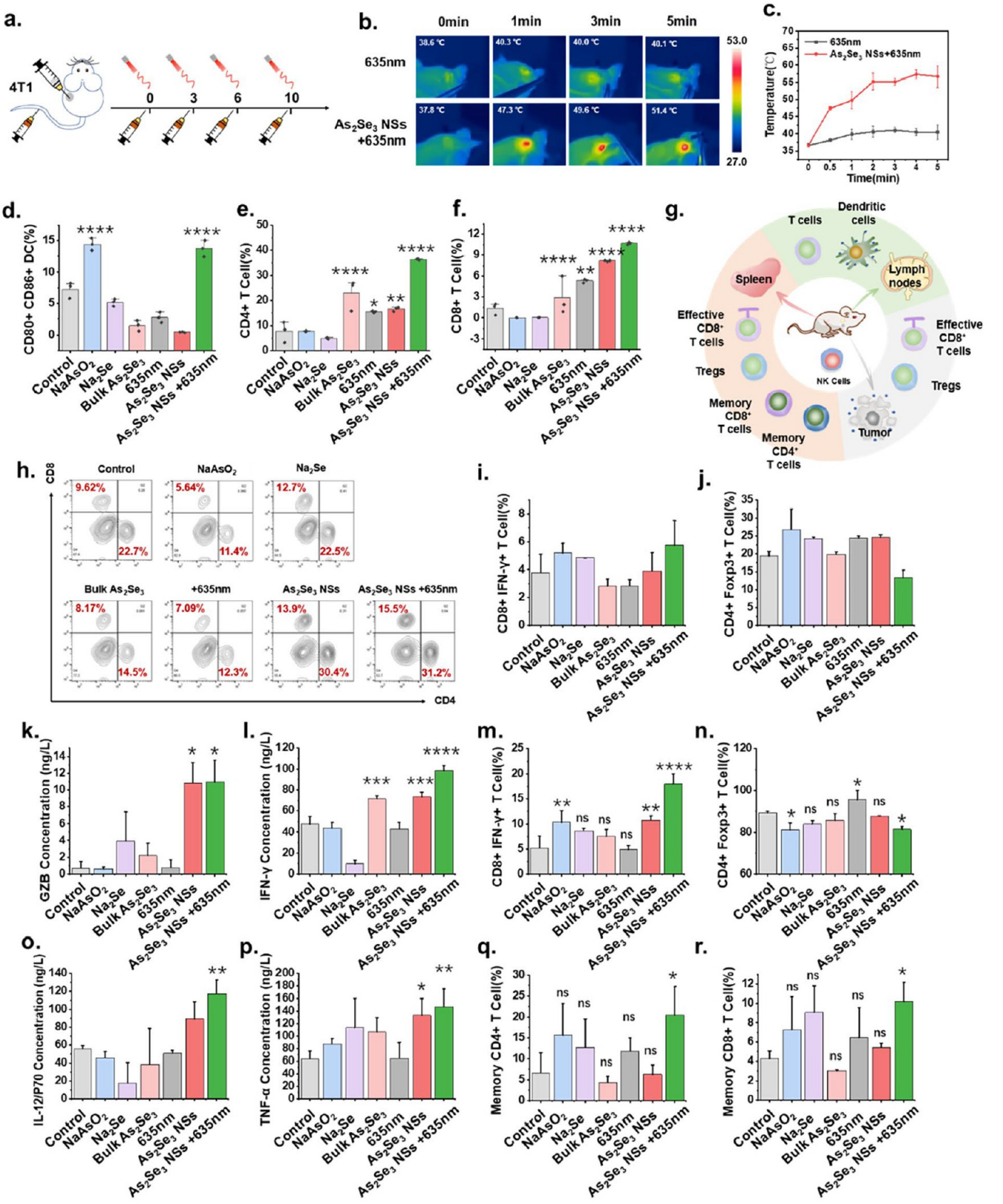

Figure 4. Photothermal and immune activation induced by As_2Se_3 NSs combined with PTT *in vivo*. (a) Schematic illustration of the therapeutic process. (b, c) NIR light (635 nm laser, 0.5 W/cm^2)-triggered photothermal conversion ability of As_2Se_3 NSs in mice. Statistical percentages of (d) CD80$^+$ and CD86$^+$ DCs, (d) CD69$^+$ CD4$^+$ T cells, and (d) CD69$^+$ CD8$^+$ T lymphocytes infiltrating lymph nodes from different groups determined by flow cytometry analysis. (g) Schematic mechanism of immune activation by As_2Se_3 NSs. (h) Statistical analysis of CD8$^+$ T cells and CD4$^+$ T cells in the spleen, (i, j) CD8$^+$/IFN-γ^+ and CD4$^+$/Foxp3$^+$ T cells in the spleen, and (m, n) CD8$^+$/IFN-γ^+ and CD4$^+$/Foxp3$^+$ T cells in the TME by flow cytometry analysis. The levels of GZB (k), IFN-γ (l), IL12/P70 (o), and TNF-α (p) in the serum of mice after different treatments. (q, r) Statistical analysis of the percentages of memory CD4$^+$ T cells and memory CD8$^+$ T cells by flow cytometry analysis. All the

https://doi.org/10.1021/acsnano.3c10432
ACS Nano 2024, 18, 4398−4413

Figure 4. continued

values are expressed as the means ± SDs of triplicate samples. Statistical significance was assessed by one-way ANOVA. $P < 0.05$ (*), $P < 0.01$ (**), $P < 0.001$ (***), or $P < 0.0001$ (****).

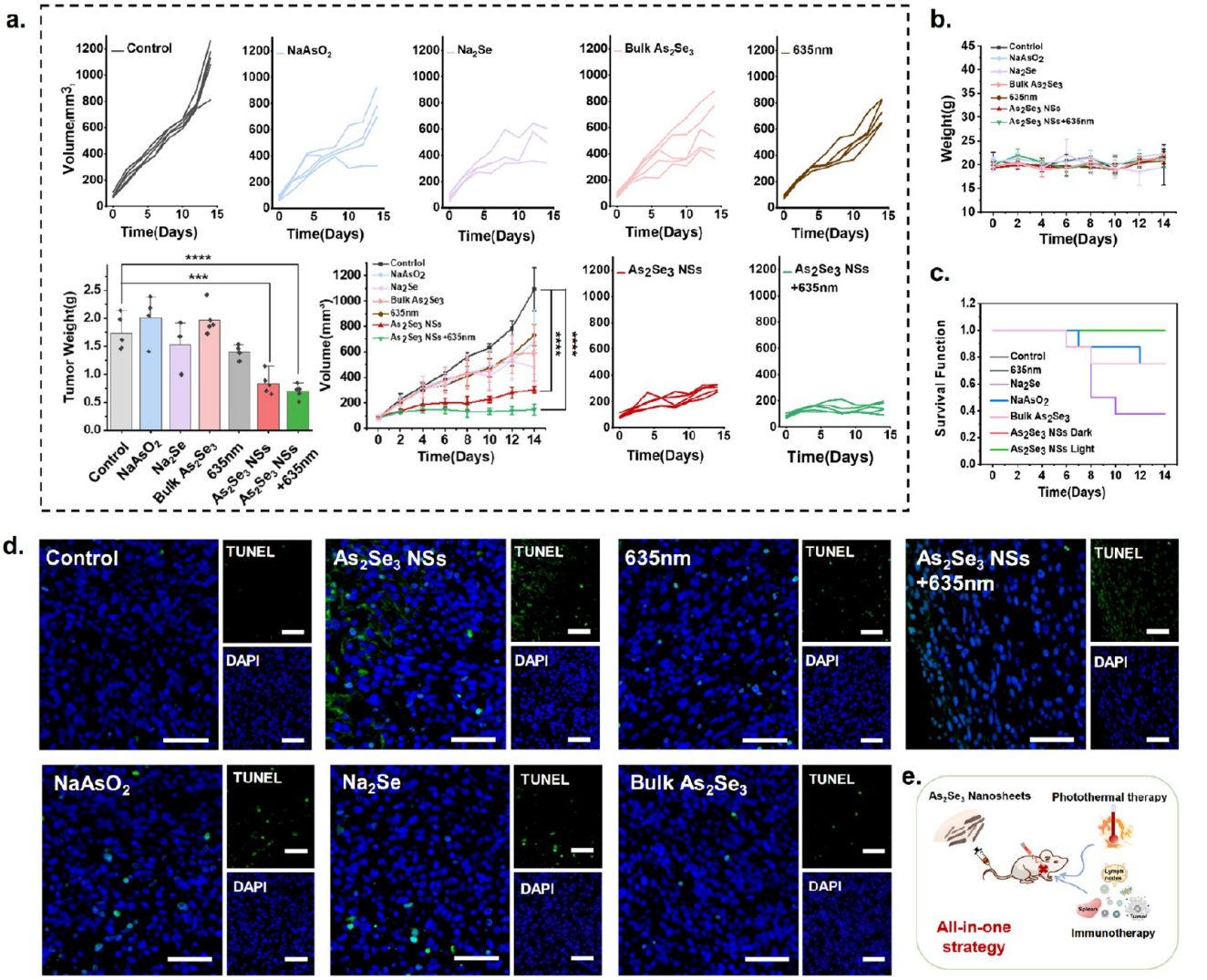

Figure 5. Antitumor effect of As_2Se_3 NSs combined with PTT *in vivo*. (a) Tumor weight and tumor volume determination after the indicated treatments ($n = 5$, mean ± SD). (b) The body weights of the mice after the indicated treatments. (c) The survival rate of tumor-bearing mice treated with different modalities. (d) TUNEL staining of tumors from mice in different treatment groups; scale bar: 50 μm. (e) Schematic of the all-in-one strategy by As_2Se_3 NSs.

treatments. These findings indicate that hyperthermia via As_2Se_3 NSs effectively improved tumor immunogenicity, facilitating the differentiation of DCs and recruiting $CD8^+$ T cells and $CD4^+$ T cells to reach tumor-draining lymph nodes and exert innate anticancer immune effects.

The detection of immune cells in the spleen and tumor microenvironment was subsequently conducted to evaluate the effect of As_2Se_3 NSs on antitumor immune activation after 14 days of treatment. Flow cytometry analysis of the spleen revealed that both As_2Se_3 NSs and As_2Se_3 NSs + 635 nm induced an increase in the number of $CD4^+$ and $CD8^+$ T cells in the spleen (Figure 4h and Figure S11). Furthermore, an increase in the $CD4^+$ T and $CD8^+$ T-cell numbers induced by As_2Se_3 NSs and As_2Se_3 NSs of +635 nm was also observed in the tumor microenvironment (TME) (Figure S12). Further analysis of the immune cell types was conducted to distinguish the immunosuppressive cells and effective immune activation cells in the TME. We next detected the subsequent effector tumor-specific $CD8^+$ T cells and Treg cells among the $CD4^+$ T cells. Our results showed that As_2Se_3 NSs+635 nm treatment significantly promoted an increase in the number of $CD8^+$/IFN-γ^+ T cells and a decrease in the number of $CD4^+$/$Foxp3^+$ Treg cells in both the tumor microenvironment and spleen (Figure 4i,j,m,n). In particular, the increase in the $CD8^+$/IFN-γ^+ T-cell population was 2.45 times greater than that induced by $NaAsO_2$ treatment (Figure S12b). Thus, the photothermal-triggered anticancer immune activation of As_2Se_3 NSs contributed to the excellent antitumor immune-modulating capabilities of As_2Se_3 NSs in activating T-cell immunity and reshaping the tumor immune microenvironment, and the

https://doi.org/10.1021/acsnano.3c10432
ACS Nano 2024, 18, 4398−4413

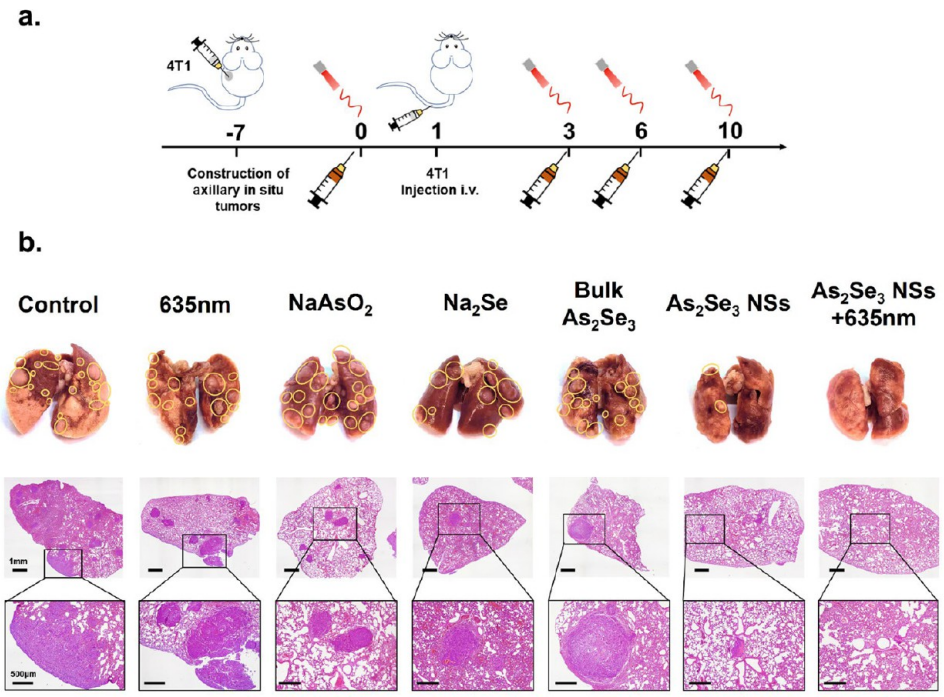

Figure 6. Antimetastatic tumor effect. (a) Schematic illustration of the antimetastatic therapeutic process. (b) Lung appearance and H&E staining after different treatments.

capabilities of As_2Se_3 NSs were superior to those of $NaAsO_2$ and Na_2Se.

In addition to T cells, natural killer (NK) cells are presumed to be key effectors of cancer immunosurveillance that spontaneously kill cancer cells.[59] NK cell-mediated tumor cell killing is dependent on granzyme B (GZB) and perforin, and the secretion of proinflammatory cytokines and chemokines (such as IFN-γ, TNF, IL-6, CCL5 and GM-CSF) by NK cells exerts direct antitumor effects and modulates the responses of dendritic cells (DCs) and T cells.[60] Therefore, the serum levels of related cytokines were measured after treatment to determine the activation of the NK cells. The increased levels of TNF-α and IFN-γ promoted NK cell activation, and the elevated levels of the tumor-killing cytokines GZB and IFN-γ secreted by NK cells after As_2Se_3 NSs+635 nm treatment confirmed the activation of NK-mediated natural immune responses, which were independent of antibodies and complement and directly killed tumor cells (Figure 4k,l,o,p).

Based on the increase in antitumor immune activation observed, we further examined the production of immunological memory cells to evaluate the formation of long-term immunological memory. The spleen cells were stained for CD3/CD4/CD62L/CD44 and CD3/CD8/CD62L/CD44, while the memory T cells were identified by low CD62L and high CD44 expression.[61,62] As shown, only As_2Se_3 NSs+635 nm treatment significantly activated the differentiation of memory $CD4^+$ T cells and $CD8^+$ T cells and further accelerated the formation of long-term immunological memory to prevent the recurrence of secondary tumors (Figure 4q,r).

Taken together, these findings suggest that treatment with As_2Se_3 NSs after irradiation first activates the differentiation of mature DCs and recruits $CD4^+$ T cells and $CD8^+$ T cells to the lymph nodes, which in turn activates the differentiation of effector $CD8^+$ T cells in the spleen and the migration of T cells to the tumor microenvironment. In addition, the innate immune response occurs via the activation of NK cells. Moreover, the significant reduction in immunosuppressive Treg cells and the effective activation of tumor-specific $CD8^+$ T cells reshaped the TME together, making cold tumors immunologically hot (Figure 4g). These results indicate that the use of selenium-containing As_2Se_3 NSs may be a potential approach for achieving simultaneous immunotherapy and photothermal therapy through a simple but effective method.

In Vivo Therapeutic Effect of As_2Se_3 NSs on Cancer Via an All-in-One Strategy. Finally, the therapeutic effect of As_2Se_3 NSs via an all-in-one strategy was investigated *in vivo*. A 4T1 tumor-bearing mouse model was constructed, and after 0, 3, 6, and 10 days of treatment with saline, $NaAsO_2$, Na_2Se, bulk As_2Se_3, As_2Se_3 NSs, 635 nm irradiation, or As_2Se_3 NSs + 635 nm irradiation at an arsenic concentration of 15 mg/kg, the mice were injected via the tail vein and observed for 14 days. The corresponding 635 nm irradiation was applied 2 h after administration to reduce metabolic loss. Through this enhanced PTT effect, the 4T1 tumor volume and weight were significantly suppressed by As_2Se_3 NSs and As_2Se_3 NSs+635 nm, while no obvious inhibition was observed in the groups treated with 635 nm, $NaAsO_2$, Na_2Se, or bulk As_2Se_3 (Figure 5a). After 14 days, the mice were sacrificed, and the tumors were separated and stained with hematoxylin-eosin (H&E) and terminal-deoxynucleotidyl transferase-mediated nick end labeling (TUNEL). Both H&E and TUNEL staining revealed significant apoptosis in tumor tissues induced by As_2Se_3 NSs after 635 nm irradiation, reflecting the high therapeutic efficacy of As_2Se_3 NSs (Figure 5d and Figure S14).

Notably, the weight of the surviving mice was not significantly affected by the treatments (Figure 5b). In terms of the survival rate of the treated mice, Na_2Se induced strong physiological toxicity *in vivo*, with a survival rate of only 37.5%, and the survival rate of mice treated with $NaAsO_2$ and bulk As_2Se_3 was 75%. Importantly, no deaths were observed in the As_2Se_3 NSs or

https://doi.org/10.1021/acsnano.3c10432
ACS Nano 2024, 18, 4398−4413

As_2Se_3 NSs + 635 nm-treated groups, further confirming the biosafety, detoxifying capability, and high therapeutic efficacy of As_2Se_3 NSs *in vivo* (Figure 5c).

Considering the remodeling of "hot" tumors and the long-term immunological memory induced by As_2Se_3 NSs + 635 nm treatments, we next elucidated the impact of the immunotherapeutic effects on 4T1 metastatic tumors. A mouse model of metastasis was generated by injecting 4T1 cells through the tail vein, after which the mice were subjected to different treatments (Figure 6a). As displayed in Figure 6b, the photographic appearance and H&E staining of lung tissues confirmed that treatment with As_2Se_3 NSs or As_2Se_3 NSs + 635 nm could significantly inhibit lung metastasis in mice, demonstrating the promising potential of As_2Se_3 NSs for preventing cancer metastasis.

Taken together, the resulting selenium-containing As_2Se_3 NSs, which are highly biocompatible and capable of detoxification, biosafety, photothermal conversion efficiency, and immune microenvironment reshaping, led to greatly enhanced chemotherapy, PTT, and immunotherapy via a simple but effective all-in-one strategy. In this work, the high efficiency of As_2Se_3 NSs enhanced the cancer photothermal immunotherapy.

CONCLUSION

In summary, in this work, by combining detoxified selenium and therapeutic arsenic, we successfully synthesized 2D ultrathin As_2Se_3 nanosheets by liquid exfoliation after high-temperature crystallization to reduce toxicity and enhance the therapeutic efficacy of arsenic treatments. Importantly, under physiological conditions, As_2Se_3 NSs can be degraded to release As(III) and Se(0), and the coexistence of Se and As reduces systematic toxicity, accelerating the rapid and efficient metabolic excretion of arsenic via blood, urine, and feces. Notably, in the liver, the selenium derived from biodegradable As_2Se_3 NSs promotes the conversion of Se to selenoenzymes, and this biotransformation of selenium to selenoenzymes GPX4 and TXNRD1 further relieves the oxidative damage induced by arsenic. In addition, the 2D structure and suitable bandgap endow As_2Se_3 NSs with excellent photothermal conversion efficiency. This hyperthermia improved tumor immunogenicity and created a favorable niche for facilitating Se-mediated immunotherapy. As_2Se_3 NSs reprogrammed the tumor microenvironment (TME) by increasing the infiltration of natural killer (NK) cells and the number of effector tumor-specific $CD8^+$ T cells, enhancing the efficacy of the TME. Mechanistically, As_2Se_3 NSs may bind to proteins involved in glycolysis, cytoskeleton regulation, and the cell cycle, affecting protein translation via photothermal-triggered cancer cell lethality. The high biocompatibility, detoxifying capability, biosafety and bioavailability, high photothermal conversion efficiency, and immune microenvironment reshaping ability of the synthesized As_2Se_3 NSs led to greatly enhanced synergistic immunotherapy and photothermal therapy via a simple but effective all-in-one strategy, developing the multifunctional therapeutic strategies for cancer therapy.

METHOD

Materials. Arsenic selenide powder (>99.999%) and Na_2Se were purchased from MERYER. $NaAsO_2$ was purchased from Sigma−Aldrich. NMP was purchased from J&K Scientific. A Cell Counting Kit-8 (CCK-8) and Annexin V-FITC/PI apoptosis detection kit were obtained from KeyGEN Biotechnology (China). Fluorochrome-conjugated antibodies, such as antimouse CD3-FITC (#100203), antimouse CD4-PE (#116005), antimouse CD8a-APC (#100712), antimouse CD11c-APC (#117310), antimouse CD80-FITC (#104705), antimouse CD86-PE (#105007), antimouse CD69-FITC (#104505), antimouse CD44-PerCP (#103035), and antimouse CD62L-APC (#104411), were purchased from BioLegend (San Diego, USA). Fluorochrome-conjugated antibodies, such as antimouse FoxP3-FITC (#11-5773-82), antimouse CD25-APC (#17-0251-81) and antimouse CD8a-PE (MA1-10304), were purchased from introvigen.

Preparation of As_2Se_3 NSs. Arsenic selenide powder (3.00 g) was crystallized at 200 °C in NaOH solution (pH 12, 27 mL) for 24 h. Then, 200 mg of As_2Se_3 was added to 100 mL of *N*-methylpyrrolidone (NMP) and sonicated in an ice bath for 4 h at 1200 W. Next, the solid obtained by centrifugation at maximum speed was further exfoliated in 25 mL of NMP for 16 h at 600 W to adjust its size and yield. Finally, the resulting brown suspension was centrifuged at 2500 rpm for 10 min to remove the residual unexfoliated particles, and the supernatant containing arsenic selenide nanosheets (As_2Se_3 NSs) was collected for further use. Importantly, ICP−MS was used to measure the concentration of As_2Se_3 NSs as a function of arsenic concentration.

Characterization of As_2Se_3 NSs. For scanning electron microscopy (SEM), transmission electron microscopy (TEM), and atomic force microscopy (AFM), the As_2Se_3 NSs were dispersed in ethyl alcohol. SEM was performed on a TESCAN MIRA LMS system with an operating voltage of 3 kV. AFM was performed on a Bruker Dimension Icon system. TEM was performed on a JEM-1200EX system. A JEOL JEM-F200 model (Japan) with an accelerating voltage of 200 kV was used for the morphological observations (high-resolution), and an energy spectrum model JED-2300T was used for the surface scanning. X-ray photoelectron spectroscopy (XPS) was performed on a Thermo Scientific K-Alpha X-ray photoelectron spectrometer with Al Kα X-ray radiation to investigate the valence state of the realgar nanocrystals. Powder X-ray diffraction (XRD) patterns were recorded on an X-ray diffractometer (Bruker D-8 Advance, Cu Kα radiation source). The different sizes of As_2Se_3 NSs were measured via DLS (Brookhaven BI-200SM).

Cell Lines. 4T1 cells (mouse breast cancer cells) were purchased from the American Type Culture Collection (Manassas, VA), authenticated by using short tandem repeat (STR) typing, and confirmed to be mycoplasma free by KeyGEN Biotech Co., Ltd. (Nanjing, China). 4T1 cells were subsequently cultured in DMEM or α-MEM (Gibco) supplemented with 10% FBS (Gibco), 100 units/ml penicillin, and 50 units/ml streptomycin at 37 °C in a CO_2 incubator (95% relative humidity, 5% CO_2).

Photothermal Effect Measurements. The photothermal effects of As_2Se_3 NSs at different concentrations (0, 3.125, 6.25, 12.5, and 25 μg/mL) and in different solutions were evaluated by using a 635 nm laser at 2.0 W/cm^2 for 10 min. Moreover, the photothermal stability of As_2Se_3 NSs for six on/off irradiation cycles was monitored. The temperature was recorded with an infrared thermal camera.

Light/Dark Cytotoxicity Analysis. The cytotoxicity of As_2Se_3 NSs on 4T1 cells was assessed by a CCK-8 assay (KeyGen). For the experiment, cells were seeded into 96-well plates at a density of approximately 5000 cells per well overnight. Then, the cells were incubated with 100 μL of fresh medium

https://doi.org/10.1021/acsnano.3c10432
ACS Nano 2024, 18, 4398−4413

(10% FBS) containing different concentrations of As_2Se_3 NSs for 48 h. The Light Experiment Group was treated with a 635 nm laser at 2.0 W/cm^2 for 10 min after incubation of As_2Se_3 NSs (As_2Se_3 NSs + 635 nm), while the Dark Experiment Group was wrapped in tin foil. Subsequently, 5 μL of a CCK-8 solution was added to each well and incubated for another 4 h. After incubation, the color intensity of the medium was measured at 450 nm using a microplate reader (Tecan Infinite M1000 PRO) to calculate the cell viability. All of the experiments were conducted three times to ensure reproducibility of the results. The cells were pretreated with the cell death inhibitor Z-VAD-FMK, the ferroptosis inhibitor Fer-1 and DFO, the necrosis inhibitor Nec-1, and the autophagy inhibitor chloroquine for 10 min.

Cell Uptake Experimentation. 4T1 cells were seeded into 6-well plates at a density of approximately 200,000 cells per well overnight. Then, the cells were incubated with 2 mL of fresh medium (10% FBS) containing 8 μg/mL As_2Se_3 NSs for 1, 3, 6, and 12 h. The cells were subsequently collected and counted, after which the arsenic and selenium concentrations were determined via ICP−MS.

Degradation Analysis of As_2Se_3 NSs in H_2O. As_2Se_3 NSs were added to ddH_2O for 0.5, 1, 2, 4, 8, 12, 24, 48, and 72 h. Next, the mixture was separated at maximum speed, and the arsenic and selenium concentrations in the supernatant were determined via ICP−MS.

Detection of Cell Apoptosis. Cell apoptosis was detected using an Annexin V-FITC Apoptosis Detection Kit (KeyGEN Biotech Co., Ltd.) following the manufacturer's protocol. Briefly, 4T1 cells were seeded onto six-well plates at 2.0 × 10^6 cells/well for 24 h. Then, 2 μg/mL As_2Se_3 NSs was added, followed by incubation for 12 h. Moreover, $NaAsO_2$, Na_2Se, and bulk As_2Se_3 were administered in equivalent proportions. For low toxicity, Na_2Se (2 μg/mL Se) and bulk As_2Se_3 (2 μg/mL As) were administered at equivalent As/Se concentrations of As_2Se_3 NSs. Specifically, for excessive toxicity, $NaAsO_2$ (1 μg/mL As) was selected for this study, which had the same effect as As_2Se_3 NSs + 635 nm (Figure 2j). After incubation at 37 °C for 12 h, the cells were collected and stained with the Annexin V-FITC apoptosis detection kit dye. Fluorescence detection was performed using the FL-1H and FL-2H channels of a flow cytometer (BD FACSCalibur).

Detection of Cellular ROS Levels. ROS levels were determined using a Reactive Oxygen Species assay kit (KeyGEN) following the manufacturer's protocol. The treatment processes were the same as those in the apoptosis assay. Then, the medium was removed, and the cells were washed 3 times with PBS and probed with 10 μM DCFH-DA in serum-free DMEM. After incubation in 5% CO_2 at 37 °C for 30 min, the cells were collected, and fluorescence was detected by using the FL-1H channel of a flow cytometer (BD FACSCalibur).

Live/Dead Cell Detection. 4T1 cells were seeded in 96-well plates at a density of approximately 10,000 cells per well and incubated overnight. The treatment processes were the same as those in the apoptosis assay. Live/dead cell detection by fluorescence microscopy (ZEISS) was performed using a live/dead double staining kit (catalog no. KGAF001, KeyGEN) according to the recommended protocol.

Valence Detection of As and Se In Vitro. 4T1 cells were seeded overnight following treatment with 15 μg/mL As_2Se_3 NSs with or without a 635 nm laser. After different incubation times, the supernatant was discarded and the cells were collected. Then, 75% ethanol was used to fix the cells for 15 min, and pure ethanol was used to dehydrate the cells for 15 min. Next, the solid was collected by centrifugation at a maximum speed. After freeze-drying, the valence states of As and Se were determined via XPS.

Binding Proteins of As_2Se_3 NSs Detected by Mass Spectrometry Analysis. As_2Se_3 NSs were mixed with the protein lysate of 4T1 cells for 24 h. Then, As_2Se_3 NSs and the binding protein of As_2Se_3 NSs were collected by centrifugation at 12,000 rpm and washed 3 times. The precipitate was separated by deformed gel electrophoresis because the As_2Se_3 NSs were too large to enter the gel. Next, the gel was stained with Coomassie blue. The entire target lane was subsequently removed; decolorization, reduction, alkylation, and trypsin enzyme digestion were performed, and the peptide sample was extracted. After spin drying, the peptide segment samples were resuspended in an aqueous solution containing 0.1% (v/v) formic acid and then analyzed by LC−MS/MS. The LC was separated by using a low-pH mobile phase, and an instrument was used to connect the Vanquish Neo liquid phase in series with an Orbitrap Explorer 480 mass spectrometer (Thermo Fisher Scientific). The mass spectrometry data were quantitatively analyzed using Thermo Proteome Discoverer 2.5.

Hemolysis Analysis. As_2Se_3 NSs were dispersed in 0.9% NaCl and mixed with 0.5 mL of red blood cells for 8 h. In addition, 0.9% NaCl solution and Triton X-100 (10 mg/mL) were used as the negative control and positive control, respectively. After incubation, the mixture was centrifuged at 3000 rpm for 10 min. Then, 100 μL of the supernatant was transferred to a 96-well plate, and the OD540 value of the samples was measured using a microplate reader (Tecan Infinite M1000 PRO). The hemolysis rate (HR) was calculated according to Formula 1

$$\mathrm{HR}(\%) = \frac{\mathrm{OD}_{\mathrm{sample}} - \mathrm{OD}_{\mathrm{negative}}}{\mathrm{OD}_{\mathrm{positive}} - \mathrm{OD}_{\mathrm{negative}}} \times 100\% \quad (1)$$

where OD is the absorbance of the sample at 540 nm.

As_2Se_3 NSs for In Vivo Photothermal Therapy of Solid Tumors. All animal experiments were performed in accordance with the National Institutes of Health animal care guidelines. Animal protocols were approved by the Institutional Animal Care and Use Committees on Animal Care (Nanjing University, IACUC-D2202146).

To establish the tumor-bearing mouse model, female BALB/c mice purchased from the Model Animal Research Center of Nanjing University (Jiangsu, China) were subcutaneously injected into the left foreleg armpit of each mouse with 1.0 × 10^6 4T1 cells in 100 μL of PBS. Tumor size was determined by a Vernier caliper at frequent intervals, and the tumor volume (V) was calculated by formula 2

$$V(\mathrm{mm}^3) = \frac{L \times W^2}{2} \quad (2)$$

where L is the length of the tumor and W is the width of the tumor. The mice were randomly divided into 7 groups (n = 5 per group).

To evaluate the *in vivo* photothermal therapeutic efficacy of As_2Se_3 NSs, As_2Se_3 NSs were administered via tail vein injection at an arsenic concentration of 15 mg/kg. After diffusion for 2 h, the tumor underwent 635 nm NIR laser irradiation (0.5 W/cm^2 for 5 min), and the corresponding temperature change was recorded using a digital infrared thermal camera. Na_2Se (15 mg/kg Se) and bulk As_2Se_3 (15 mg/kg As) were administered at

https://doi.org/10.1021/acsnano.3c10432
ACS Nano 2024, 18, 4398−4413

equivalent As/Se concentrations. For excessive toxicity, 3 mg/kg As in $NaAsO_2$ was chosen as the relatively effective and safe concentration.[63]

After 0, 3, 6, or 10 days of treatment, the antitumor effect was tested on the 14th day due to the large tumor volume in the control group. Changes in body weight and tumor size were measured for 14 days. Moreover, the survival of tumor-bearing mice treated with different modalities was monitored. On day 14, the mice were euthanized, and the tumor tissue was collected and fixed with 10% neutral buffered formalin. Then, the tumors were embedded in paraffin, processed into 100 μm sections, and stained with hematoxylin and eosin (H&E). The images were obtained by digital microscopy. In addition, tumor tissue was collected on day 14 for terminal deoxynucleotidyl transferase-mediated dUTP nick end labeling (TUNEL) staining.

In Vivo Toxicity of As_2Se_3 NSs. Blood was collected from mice in different treatment groups for hematological analysis and serum biochemistry assays. Hematological analysis was performed on a Photoelectric MEK-8222K automatic five-class blood cell analyzer instrument. Serum biochemistry assays were performed using an associated assay kit (Nanjing Jiancheng Bioengineering Institute, China). The major organs (liver, spleen, kidney, heart, and lung) were harvested, fixed in 10% neutral buffered formalin, processed routinely into paraffin-embedded sections, stained with hematoxylin and eosin, and examined by digital microscopy.

In Vivo Biotransformation of As_2Se_3 NSs. As_2Se_3 NSs were administered via tail vein injection at an arsenic concentration of 15 mg/kg, with 0.9% NaCl serving as a control. After treatment for 1, 3, and 7 days, the livers of the mice were collected and ground into a homogenate. Total protein was subsequently extracted from the tissue homogenate (BestBio BB-3101). The protein concentration was determined by the Super-Bradford Protein Assay Kit (CWBiotech, Inc., Beijing, China). The extracts were first separated by SDS−PAGE and subsequently transferred to a poly(vinylidene difluoride) membrane (Bio-Rad, CA, USA). The membrane was blocked with 4% BSA in TBST at 25 °C for 2 h and then incubated with antibodies at 4 °C overnight. The expression of GAPDH was used as the internal standard. Primary antibodies against the following proteins were used: GAPDH (ab8245, 1:1000 for WB) from Abcam, GPX4 (ab125066, 1:1000 for WB) from Abcam, and TXNRD1 (ab124954, 1:1000 for WB) from Abcam. The appropriate secondary antibodies (1:1000 for WB) were purchased from CST.

DC and T-Cell Stimulation of As_2Se_3 NSs In Vivo. The mouse model was established as above, and the lymph nodes in the tumor-draining area were removed after the mice were sacrificed 24 h after intravenous injection. Then, the lymph nodes were sieved, treated with erythrocyte lysate, and centrifuged to obtain a cell suspension. The cell suspension was subjected to anti-CD11c APC, anti-CD86 PE, and anti-CD80 FITC antibodies and analyzed via flow cytometry to detect DCs. In addition, the cell suspension was subjected to anti-CD69 FITC, anti-CD4 PE, and anti-CD8 APC antibodies to detect T cells.

Immune Activation Detection of As_2Se_3 NSs In Vivo. The mouse model was established as described above, and the mouse spleens and tumors were dissected on day 14. The cell suspension was subjected to anti-CD3 FITC, anti-CD4 PE, and anti-CD8 APC antibodies and analyzed via flow cytometry. Next, anti-CD3 FITC, anti-CD8a PE, and anti-IFN-γ APC antibodies were used to stain the cell suspension, and the cell suspension was analyzed by flow cytometry to detect effector tumor-specific $CD8^+$ T cells. Anti-CD4 PE and anti-Foxp3 FITC antibodies were used to stain the cell suspension to distinguish Tregs. Anti-CD25 APC was used to assist in identifying Tregs in the spleen. Moreover, serum samples were collected for cytokine detection. The levels of IL-12p70, IFN-γ, GZB, and TNF-α were measured with ELISA kits.

Immune Memory Detection of As_2Se_3 NSs In Vivo. The mouse model was established as described above, and the mouse spleens were dissected on day 14. After staining with anti-CD3 FITC, anti-CD8 PE/anti-CD4 PE, anti-CD44 PerCP, and anti-CD62L APC antibodies, changes in central memory and effector memory T-cell numbers were determined by flow cytometry.

In Vivo 4T1 Tumor Metastasis Model. To establish the tumor-bearing mouse model, BALB/c mice were subcutaneously injected with 1.0×10^6 4T1 cells in the left foreleg armpit. After 7 days of *in situ* tumor establishment, BALB/c mice were intravenously injected with different treatments. After 24 h, 1.0×10^6 4T1 cells were intravenously injected to establish a metastasis model. After 18 days of treatment, the mice were sacrificed, and the lungs were harvested. Lung tissues were then collected and stained with hematoxylin and eosin (H&E).

The Metabolism and Enrichment of As_2Se_3 NSs In Vivo. For the blood circulation assay, a 10 μL blood sample was obtained from mice 0, 0.5, 1, 3, 6, 12, 24, 48, and 72 h after intravenous injection of As_2Se_3 NSs. Similarly, the urine and feces of the mice were collected at the same time points for metabolic assessment. The organs were collected at 12, 24, 48, and 72 h for enrichment assessment. The concentrations of As and Se were determined via ICP−MS.

Statistical Analysis. All the data are expressed as the mean ± standard deviation. One-way analysis of variance (ANOVA) was used for multiple group comparisons. All the statistical analyses were performed using GraphPad Prism 9.0. Differences with $P < 0.05$ (*), $P < 0.01$ (**), $P < 0.001$ (***), or $P < 0.0001$ (****) were considered to indicate statistical significance.

ASSOCIATED CONTENT

Supporting Information

The Supporting Information is available free of charge at https://pubs.acs.org/doi/10.1021/acsnano.3c10432.

Zeta potential, photothermal effects, degradation and semiquantitative analysis by EDS and ICP−MS of As_2Se_3 NSs; cytotoxicity in the control group; mass spectrometry data analysis of As_2Se_3 NSs; flow cytometry assay (Figure 4); organ weight after different treatments; distribution of selenium in organs; metabolization of As_2Se_3 NSs *in vivo*; and H&E staining of tumors from mice subjected to different treatments (PDF)

AUTHOR INFORMATION

Corresponding Authors

Xiuxiu Wang − *Chemistry and Biomedicine Innovation Center (ChemBIC), State Key Laboratory of Coordination Chemistry, School of Chemistry and Chemical Engineering, Nanjing University, Nanjing 210023, China*; Email: wangxiuxiu@nju.edu.cn

Jing Zhao − *Chemistry and Biomedicine Innovation Center (ChemBIC), State Key Laboratory of Coordination Chemistry, School of Chemistry and Chemical Engineering, Nanjing University, Nanjing 210023, China*; Email: jingzhao@nju.edu.cn

https://doi.org/10.1021/acsnano.3c10432
ACS Nano 2024, 18, 4398−4413

Wei Wei − *School of Life Sciences, Nanjing University, Nanjing 210023, China;* orcid.org/0000-0003-0845-0527; Email: weiwei@nju.edu.cn

Authors

Jingyi Zhang − *Chemistry and Biomedicine Innovation Center (ChemBIC), State Key Laboratory of Coordination Chemistry, School of Chemistry and Chemical Engineering, Nanjing University, Nanjing 210023, China*

Yue Qin − *Chemistry and Biomedicine Innovation Center (ChemBIC), State Key Laboratory of Coordination Chemistry, School of Chemistry and Chemical Engineering, Nanjing University, Nanjing 210023, China*

Yiming Chen − *School of Engineering, Vanderbilt University, Nashville 37235-0734 Tennessee, United States*

Xinyang Zhao − *Chemistry and Biomedicine Innovation Center (ChemBIC), State Key Laboratory of Coordination Chemistry, School of Chemistry and Chemical Engineering, Nanjing University, Nanjing 210023, China*

Jing Wang − *Chemistry and Biomedicine Innovation Center (ChemBIC), State Key Laboratory of Coordination Chemistry, School of Chemistry and Chemical Engineering, Nanjing University, Nanjing 210023, China*

Zhenzhen Wang − *School of Life Sciences, Nanjing University, Nanjing 210023, China*

Jiayi Li − *School of Life Sciences, Nanjing University, Nanjing 210023, China*

Jing Zhao − *School of Life Sciences, Nanjing University, Nanjing 210023, China*

Shengjin Liu − *College of Pharmacy, Nanjing University of Chinese Medicine, Nanjing 210023, China*

Zijian Guo − *Chemistry and Biomedicine Innovation Center (ChemBIC), State Key Laboratory of Coordination Chemistry, School of Chemistry and Chemical Engineering, Nanjing University, Nanjing 210023, China;* orcid.org/0000-0003-4986-9308

Complete contact information is available at: https://pubs.acs.org/10.1021/acsnano.3c10432

Notes

The authors declare no competing financial interest.

ACKNOWLEDGMENTS

This work was supported by the National Natural Science Foundation of China (22207053, 22025701, 22177048, 92353301, and 22101129), the National Key R&D Program of China (2023YFA1508900), the Natural Science Foundation of Jiangsu Province (BK20220764 and BK20202004), and the 2021 Strategic Research Project of the Science and Technology Commission of the Ministry of Education of China.

ABBREVIATIONS

APL, acute promyelocytic leukemia; As_2Se_3 NSs, As_2Se_3 nanosheets; NK cells, natural killer cells; PLGA, poly(lactic-*co*-glycolic acid); 2D, two-dimensional; PTT, photothermal therapy; TIL, tumor-infiltrating lymphocyte; TME, tumor microenvironment; NMP, *N*-methylpyrrolidone; TEM, transmission electron microscopy; DLS, dynamic light scattering; AFM, atomic force microscopy; XRD, X-ray diffraction; JCPDS, Joint Committee on Powder Diffraction Standards; XPS, X-ray photoelectron spectroscopy; EDS, energy dispersive spectroscopy; ICP−MS, Inductive Coupled Plasma Mass Spectrometer; UV spectrum, ultraviolet and visible spectrum; PI value, phototoxic index value; H&E staining, hematoxylin and eosin staining; DCs, dendritic cells; GZB, granzyme B; TUNEL, terminal-deoxynucleotidyl transferase-mediated nick end labeling

REFERENCES

(1) Zhu, J.; Chen, Z.; Lallemand-Breitenbach, V.; de The, H. How Acute Promyelocytic Leukaemia Revived Arsenic. *Nat. Rev. Cancer.* **2002**, *2* (9), 705−713.

(2) Zhu, H. H.; Hu, J.; Lo-Coco, F.; Jin, J. The Simpler, the Better: Oral Arsenic for Acute Promyelocytic Leukemia. *Blood* **2019**, *134* (7), 597−605.

(3) Wang, Z. Y.; Chen, Z. Acute Promyelocytic Leukemia: from Highly Fatal to Highly Curable. *Blood* **2008**, *111* (5), 2505−2515.

(4) Burnett, A. K.; Russell, N. H.; Hills, R. K.; Bowen, D.; Kell, J.; Knapper, S.; Morgan, Y. G.; Lok, J.; Grech, A.; Jones, G.; Khwaja, A.; Friis, L.; McMullin, M. F.; Hunter, A.; Clark, R. E.; Grimwade, D. Arsenic Trioxide and All-Trans Retinoic Acid Treatment for Acute Promyelocytic Leukaemia in All Risk Groups (AML17): Results of a Randomised, Controlled, Phase 3 Trial. *Lancet. Oncol.* **2015**, *16* (13), 1295−1305.

(5) Oremland, R. S.; Stolz, J. F. The Ecology of Arsenic. *Science* **2003**, *300* (5621), 939−44.

(6) Duenas-Laita, A.; Perez-Miranda, M.; Gonzalez-Lopez, M. A.; Martin-Escudero, J. C.; Ruiz-Mambrilla, M.; Blanco-Varela, J. Acute Arsenic Poisoning. *Lancet* **2005**, *365* (9475), 1982.

(7) Camacho, L. H.; Soignet, S. L.; Chanel, S.; Ho, R.; Heller, G.; Scheinberg, D. A.; Ellison, R.; Warrell, R. P. Jr.; Leukocytosis and The Retinoic Acid Syndrome in Patients with Acute Promyelocytic Leukemia Treated with Arsenic Trioxide. *J. Clin. Oncol.* **2000**, *18* (13), 2620−5.

(8) Lo-Coco, F.; Avvisati, G.; Vignetti, M.; Thiede, C.; Orlando, S. M.; Iacobelli, S.; Ferrara, F.; Fazi, P.; Cicconi, L.; Di Bona, E.; Specchia, G.; Sica, S.; Divona, M.; Levis, A.; Fiedler, W.; Cerqui, E.; Breccia, M.; Fioritoni, G.; Salih, H. R.; Cazzola, M.; et al. Retinoic Acid and Arsenic Trioxide for Acute Promyelocytic Leukemia. *N. Engl. J. Med.* **2013**, *369* (2), 111−21.

(9) Zhao, Z.; Wang, X.; Zhang, Z.; Zhang, H.; Liu, H.; Zhu, X.; Li, H.; Chi, X.; Yin, Z.; Gao, J. Real-Time Monitoring of Arsenic Trioxide Release and Delivery by Activatable T(1) Imaging. *ACS Nano* **2015**, *9* (3), 2749−59.

(10) Zhang, K.; Lin, H.; Mao, J.; Luo, X.; Wei, R.; Su, Z.; Zhou, B.; Li, D.; Gao, J.; Shan, H. An Extracellular pH-Driven Targeted Multifunctional Manganese Arsenite Delivery System for Tumor Imaging and Therapy. *Biomater. Sci.* **2019**, *7* (6), 2480−2490.

(11) Song, X. L.; You, J.; Shao, H. X.; Yan, C. F. Effects of Surface Modification of As_2O_3-Loaded PLGA Nanoparticles on Its Anti-Liver Cancer Ability: An *in Vitro* and *in Vivo* Study. *Colloid Surf. B-Biointerfaces* **2018**, *169*, 289−297.

(12) Wang, C.; Zhang, W.; He, Y.; Gao, Z.; Liu, L.; Yu, S.; Hu, Y.; Wang, S.; Zhao, C.; Li, H.; Shi, J.; Zhou, W.; Li, F.; Yue, H.; Li, Y.; Wei, W.; Ma, G.; Ma, D. Ferritin-Based Targeted Delivery of Arsenic to Diverse Leukaemia Types Confers Strong Anti-Leukaemia Therapeutic Effects. *Nat. Nanotechnol.* **2021**, *16* (12), 1413−1423.

(13) Kong, N.; Zhang, H.; Feng, C.; Liu, C.; Xiao, Y.; Zhang, X.; Mei, L.; Kim, J. S.; Tao, W.; Ji, X. Arsenene-Mediated Multiple Independently Targeted Reactive Oxygen Species Burst for Cancer Therapy. *Nat. Commun.* **2021**, *12* (1), 4777.

(14) Liu, C.; Sun, S.; Feng, Q.; Wu, G.; Wu, Y.; Kong, N.; Yu, Z.; Yao, J.; Zhang, X.; Chen, W.; Tang, Z.; Xiao, Y.; Huang, X.; Lv, A.; Yao, C.; Cheng, H.; Wu, A.; Xie, T.; Tao, W. Arsenene Nanodots with Selective Killing Effects and their Low-Dose Combination with ss-Elemene for Cancer Therapy. *Adv. Mater.* **2021**, *33* (37), No. e2102054.

(15) Wang, X.; Hu, Y.; Mo, J.; Zhang, J.; Wang, Z.; Wei, W.; Li, H.; Xu, Y.; Ma, J.; Zhao, J.; Jin, Z.; Guo, Z. Arsenene: A Potential Therapeutic Agent for Acute Promyelocytic Leukaemia Cells by Acting on Nuclear Proteins. *Angew. Chem.-Int. Ed.* **2020**, *59* (13), 5151−5158.

(16) Wang, X.; Zhang, J.; Hu, Y.; Zhao, X.; Wang, Z.; Zhang, W.; Liang, J.; Yu, W.; Tian, T.; Zhou, H.; Li, J.; Liu, S.; Zhao, J.; Jin, Z.; Wei, W.; Guo, Z. Multi-Omics Analysis Reveals the Unexpected Immune Regulatory Effects of Arsenene Nanosheets in Tumor Microenvironment. *ACS Appl. Mater. Interfaces* **2022**, *14* (40), 45137−45148.
(17) Chaudhary, S.; Umar, A.; Mehta, S. K. Selenium nanomaterials: An Overview of Recent Developments in Synthesis, Properties and Potential Applications. *Prog. Mater. Sci.* **2016**, *83*, 270−329.
(18) Moxon, A. L. The Effect of Arsenic on the Toxicity of Seleniferous Grains. *Science* **1938**, *88* (2273), 81.
(19) Csanaky, I.; Gregus, Z. Effect of Selenite on the Disposition of Arsenate and Arsenite in Rats. *Toxicology* **2003**, *186* (1−2), 33−50.
(20) Levander, O. A. Metabolic Interrelationships between Arsenic and Selenium. *Environ. Health. Persp.* **1977**, *19* (Aug), 159−164.
(21) Gao, S.; Li, T.; Guo, Y.; Sun, C.; Xianyu, B.; Xu, H. Selenium-Containing Nanoparticles Combine the NK Cells Mediated Immunotherapy with Radiotherapy and Chemotherapy. *Adv. Mater.* **2020**, *32* (12), No. e1907568.
(22) Zhu, K.; Yang, S.; Li, T.; Huang, X.; Dong, Y.; Wang, P.; Huang, J. Advances in the Study of the Mechanism by Which Selenium and Selenoproteins Boost Immunity to Prevent Food Allergies. *Nutrients* **2022**, *14* (15), 3133.
(23) Avery, J. C.; Hoffmann, P. R. Selenium, Selenoproteins, and Immunity. *Nutrients* **2018**, *10* (9), 1203.
(24) Chen, M.; Cao, W.; Wang, J.; Cai, F.; Zhu, L.; Ma, L.; Chen, T. Selenium Atom-Polarization Effect Determines TrxR-Specific Recognition of Metallodrugs. *J. Am. Chem. Soc.* **2022**, *144* (45), 20825−20833.
(25) Xie, B.; Zeng, D. L.; Yang, M. J.; Tang, Z. Y.; He, L. Z.; Chen, T. F. Translational Selenium Nanoparticles to Attenuate Allergic Dermatitis through Nrf2-Keap1-Driven Activation of Selenoproteins. *ACS Nano* **2023**, *17* (14), 14053−14068.
(26) Deng, B.; He, X. M.; Wang, D. D.; Wang, Y.; Jiang, Y. L.; Chen, T. F.; Xu, L. G. Designing Selenium Nanoadjuvant as Universal Agent for Live-Killed Virus-Based Vaccine. *Small Methods* **2023**, *7*, 2300293.
(27) Chang, Y. Z.; Huang, J. R.; Shi, S. J.; Xu, L. G.; Lin, H.; Chen, T. F. Precise Engineering of a Se/Te Nanochaperone for Reinvigorating Cancer Radio-Immunotherapy. *Adv. Mater.* **2023**, *35*, 2212178.
(28) Wang, J.; Chang, Y. Z.; Luo, H.; Jiang, W. X.; Xu, L. G.; Chen, T. F.; Zhu, X. Q. Designing Immunogenic Nanotherapeutics for Photothermal-triggered Immunotherapy Involving Reprogramming Immunosuppression and Activating Systemic Antitumor Responses. *Biomaterials* **2020**, *255*, 120153.
(29) Ling, J. B.; Chang, Y. Z.; Yuan, Z. W.; Chen, Q.; He, L. Z.; Chen, T. F. Designing Lactate Dehydrogenase-Mimicking SnSe Nanosheets To Reprogram Tumor-Associated Macrophages for Potentiation of Photothermal Immunotherapy. *Acs Appl. Mater. Interfaces* **2022**, *14* (24), 27651−27665.
(30) Mortazavi, B.; Shojaei, F.; Azizi, M.; Rabczuk, T.; Zhuang, X. Y. As_2S_3, As_2Se_3 and As_2Te_3 Nanosheets: Superstretchable Semiconductors with Anisotropic Carrier Mobilities and Optical Properties. *J. Mater. Chem. C* **2020**, *8* (7), 2400−2410.
(31) Gao, W. W.; Chelikowsky, J. R. Prediction of Intrinsic Ferroelectricity and Large Piezoelectricity in Monolayer Arsenic Chalcogenides. *Nano Lett.* **2020**, *20* (11), 8346−8352.
(32) Miao, N. H.; Zhou, J.; Sa, B. S.; Xu, B.; Sun, Z. M. Few-Layer Arsenic Trichalcogenides: Emerging Two-Dimensional Semiconductors with Tunable Indirect-Direct Band-Gaps. *J. Alloy. Compd.* **2017**, *699*, 554−560.
(33) Stergiou, A. C.; Rentzeperis, P. J. The Crystal-Structure of Arsenic Selenide, As_2Se_3. *Z. Kristallogr.* **1985**, *173* (3−4), 185−191.
(34) Savitskii, I. V.; Shpotyuk, O. I.; Kornelyuk, V. N.; Matkovskii, A. O. Radiation-Stimulated Changes of Spectral Characteristics of the Transmission of Arsenic Selenide Electrophotographic Layers. *Zhurnal Nauchnoi Prikl. Fotogr.* **1987**, *32* (4), 281−285.
(35) Yang, Y.; Hu, T. T.; Bian, Y. X.; Meng, F. Q.; Yu, S. L.; Li, H.; Zhang, Q. H.; Gu, L.; Weng, X. S.; Tan, C. L.; Liang, R. Z. Coupling Probiotics with 2D CoCuMo-LDH Nanosheets as a Tumor-Microenvironment-Responsive Platform for Precise NIR-II Photodynamic Therapy. *Adv. Mater.* **2023**, *35* (23), 2211205.
(36) Hu, T. T.; Shen, W. C.; Meng, F. Q.; Yang, S. Q.; Yu, S. L.; Li, H.; Zhang, Q. H.; Gu, L.; Tan, C. L.; Liang, R. Z. Boosting the Sonodynamic Cancer Therapy Performance of 2D Layered Double Hydroxide Nanosheet-Based Sonosensitizers *Via* Crystalline-to-Amorphous Phase Transformation. *Adv. Mater.* **2023**, *35* (17), 2209692.
(37) Li, B. J.; Lv, Y. K.; Wang, Z. D.; Peng, P.; Zang, S. Q. Edge Confined Covalent Organic Framework with Efficient Biocompatibility and Photothermic Conversion. *Nano Today* **2021**, *37*, 101101.
(38) Zhang, S.; Yan, Z.; Li, Y.; Chen, Z.; Zeng, H. Atomically Thin Arsenene and Antimonene: Semimetal-Semiconductor and Indirect-Direct Band-Gap Transitions. *Angew. Chem.-Int. Ed.* **2015**, *54* (10), 3112−5.
(39) Mayorga-Martinez, C. C.; Gusmao, R.; Sofer, Z.; Pumera, M. Pnictogen-Based Enzymatic Phenol Biosensors: Phosphorene, Arsenene, Antimonene, and Bismuthene. *Angew. Chem.-Int. Ed.* **2019**, *58* (1), 134−138.
(40) Badalov, S. V.; Kandemir, A.; Sahin, H. Monolayer $AsTe_2$: Stable Robust Metal in 2D, 1D and 0D. *ChemPhysChem* **2018**, *19* (17), 2176−2182.
(41) Hu, Y.; Liang, J.; Xia, Y.; Zhao, C.; Jiang, M.; Ma, J.; Tie, Z.; Jin, Z. 2D Arsenene and Arsenic Materials: Fundamental Properties, Preparation, and Applications. *Small* **2022**, *18* (9), No. e2104556.
(42) Liu, C.; Sun, S.; Feng, Q.; Wu, G. W.; Wu, Y. T.; Kong, N.; Yu, Z. S.; Yao, J. L.; Zhang, X. C.; Chen, W.; Tang, Z. M.; Xiao, Y. F.; Huang, X. G.; Lv, A.; Yao, C. Y.; Cheng, H. B.; Wu, A. G.; Xie, T.; Tao, W. Arsenene Nanodots with Selective Killing Effects and their Low-Dose Combination with ss-Elemene for Cancer Therapy. *Adv. Mater.* **2021**, *33* (37), 2102054.
(43) Huang, H.; Feng, W.; Chen, Y. Two-Dimensional Biomaterials: Material Science, Biological Effect and Biomedical Engineering Applications. *Chem. Soc. Rev.* **2021**, *50* (20), 11381−11485.
(44) Cui, X. M.; Ruan, Q. F.; Zhuo, X. L.; Xia, X. Y.; Hu, J. T.; Fu, R. F.; Li, Y.; Wang, J. F.; Xu, H. X. Photothermal Nanomaterials: A Powerful Light-to-Heat Converter. *Chem. Rev.* **2023**, *123* (11), 6891−6952.
(45) Castellanos-Gomez, A. Black Phosphorus: Narrow Gap, Wide Applications. *J. Phys. Chem. Lett.* **2015**, *6* (21), 4280−4291.
(46) Wu, M. M.; Niu, X. M.; Zhang, R.; Xu, Z. P. Two-Dimensional Nanomaterials for Tumor Microenvironment Modulation and Anticancer Therapy. *Adv. Drug. Deliver. Rev.* **2022**, *187*, 114360.
(47) Alzakia, F. I.; Tan, S. C. Liquid-Exfoliated 2D Materials for Optoelectronic Applications. *Adv. Sci.* **2021**, *8* (11), No. 2003864, DOI: 10.1002/advs.202003864.
(48) Coleman, J. N.; Lotya, M.; O'Neill, A.; Bergin, S. D.; King, P. J.; Khan, U.; Young, K.; Gaucher, A.; De, S.; Smith, R. J.; Shvets, I. V.; Arora, S. K.; Stanton, G.; Kim, H. Y.; Lee, K.; Kim, G. T.; Duesberg, G. S.; Hallam, T.; Boland, J. J.; Wang, J. J.; et al. Two-Dimensional Nanosheets Produced by Liquid Exfoliation of Layered Materials. *Science* **2011**, *331* (6017), 568−571.
(49) Zhang, S.; Xie, M.; Li, F.; Yan, Z.; Li, Y.; Kan, E.; Liu, W.; Chen, Z.; Zeng, H. Semiconducting Group 15 Monolayers: A Broad Range of Band Gaps and High Carrier Mobilities. *Angew. Chem.-Int. Ed.* **2016**, *55* (5), 1666−9.
(50) Xi, D.; Xiao, M.; Cao, J.; Zhao, L.; Xu, N.; Long, S.; Fan, J.; Shao, K.; Sun, W.; Yan, X.; Peng, X. NIR Light-Driving Barrier-Free Group Rotation in Nanoparticles with an 88.3% Photothermal Conversion Efficiency for Photothermal Therapy. *Adv. Mater.* **2020**, *32* (11), No. e1907855.
(51) Li, S.; Deng, Q.; Zhang, Y.; Li, X.; Wen, G.; Cui, X.; Wan, Y.; Huang, Y.; Chen, J.; Liu, Z.; Wang, L.; Lee, C. S. Rational Design of Conjugated Small Molecules for Superior Photothermal Theranostics in the NIR-II Biowindow. *Adv. Mater.* **2020**, *32* (33), No. e2001146.
(52) Ouyang, J.; Feng, C.; Ji, X.; Li, L.; Gutti, H. K.; Kim, N. Y.; Artzi, D.; Xie, A.; Kong, N.; Liu, Y. N.; Tearney, G. J.; Sui, X.; Tao, W.; Farokhzad, O. C. 2D Monoelemental Germanene Quantum Dots: Synthesis as Robust Photothermal Agents for Photonic Cancer Nanomedicine. *Angew. Chem.-Int. Ed.* **2019**, *58* (38), 13405−13410.

(53) Sung, H.; Ferlay, J.; Siegel, R. L.; Laversanne, M.; Soerjomataram, I.; Jemal, A.; Bray, F. Global Cancer Statistics 2020: GLOBOCAN Estimates of Incidence and Mortality Worldwide for 36 Cancers in 185 Countries. *CA-Cancer J. Clin.* **2021**, *71* (3), 209−249.
(54) Hunt, C. R.; Parsian, A. J.; Goswami, P. C.; Kozak, C. A. Characterization and Expression of the Mouse Hsc70 Gene. *BIOCHIM BIOPHYS ACTA* **1999**, *1444* (3), 315−25.
(55) Tamura, T.; Stadtman, T. C. A New Selenoprotein from Human Lung Adenocarcinoma Cells: Purification, Properties, and Thioredoxin Reductase Activity. *Proc. Natl. Acad. Sci. U. S. A.* **1996**, *93* (3), 1006−11.
(56) Yang, W. S.; SriRamaratnam, R.; Welsch, M. E.; Shimada, K.; Skouta, R.; Viswanathan, V. S.; Cheah, J. H.; Clemons, P. A.; Shamji, A. F.; Clish, C. B.; Brown, L. M.; Girotti, A. W.; Cornish, V. W.; Schreiber, S. L.; Stockwell, B. R. Regulation of Ferroptotic Cancer Cell Death by GPX4. *Cell* **2014**, *156* (1−2), 317−331.
(57) Pan, J.; Xu, Y.; Wu, Q.; Hu, P.; Shi, J. Mild Magnetic Hyperthermia-Activated Innate Immunity for Liver Cancer Therapy. *J. Am. Chem. Soc.* **2021**, *143* (21), 8116−8128.
(58) Wang, M.; Chang, M.; Zheng, P.; Sun, Q.; Wang, G.; Lin, J.; Li, C. A Noble AuPtAg-GOx Nanozyme for Synergistic Tumor Immunotherapy Induced by Starvation Therapy-Augmented Mild Photothermal Therapy. *Adv. Sci.* **2022**, *9* (31), No. e2202332.
(59) Vivier, E.; Tomasello, E.; Baratin, M.; Walzer, T.; Ugolini, S. Functions of Natural Killer Cells. *Nat. Immunol.* **2008**, *9* (5), 503−510.
(60) Guillerey, C.; Huntington, N. D.; Smyth, M. J. Targeting Natural Killer Cells in Cancer Immunotherapy. *Nat. Immunol.* **2016**, *17* (9), 1025−1036.
(61) Yue, W.; Chen, L.; Yu, L.; Zhou, B.; Yin, H.; Ren, W.; Liu, C.; Guo, L.; Zhang, Y.; Sun, L.; Zhang, K.; Xu, H.; Chen, Y. Checkpoint Blockade and Nanosonosensitizer-Augmented Noninvasive Sonodynamic Therapy Combination Reduces Tumour Growth and Metastases in Mice. *Nat. Commun.* **2019**, *10* (1), 2025.
(62) Xu, J.; Xu, L.; Wang, C.; Yang, R.; Zhuang, Q.; Han, X.; Dong, Z.; Zhu, W.; Peng, R.; Liu, Z. Near-Infrared-Triggered Photodynamic Therapy with Multitasking Upconversion Nanoparticles in Combination with Checkpoint Blockade for Immunotherapy of Colorectal Cancer. *ACS Nano* **2017**, *11* (5), 4463−4474.
(63) Mathas, S.; Lietz, A.; Janz, M.; Hinz, M.; Jundt, F.; Scheidereit, C.; Bommert, K.; Dorken, B. Inhibition of NF-KappaB Essentially Contributes to Arsenic-Induced Apoptosis. *Blood* **2003**, *102* (3), 1028−34.

https://doi.org/10.1021/acsnano.3c10432
ACS Nano 2024, 18, 4398−4413